Understanding of interfacial molecular interactions and inner-sphere reaction mechanism in heterogeneous Fenton-like catalysis on Mn-N$_4$ site

Pijun Duan [a,b], Mingxue Li [c], Xing Xu [a], Qinyan Yue [a], Yue Gao [a,*], Baoyu Gao [a,*]

[a] *Shandong Key Laboratory of Water Pollution Control and Resource Reuse, School of Environmental Science and Engineering, Shandong University, Qingdao 266237, PR China*
[b] *Key Laboratory of the Three Gorges Reservoir Region's Eco-Environment, Ministry of Education, College of Environment and Ecology, Chongqing University, Chongqing 400045 PR China*
[c] *Environment Research Institute, Shandong University, Qingdao 266237, PR China*

ABSTRACT

This study investigated interface molecular interactions between atomically-dispersed active sites and reactants in Fenton-like catalysis for deep understanding catalytic mechanism and dynamics. N-doped carbon nanotubes (NCNTs), atomically-dispersed Mn onto NCNTs (Mn$_{sa}$-NCNT) and peroxymonosulfate (PMS) were applied as the research platforms. PMS adsorption on atomically-dispersed Mn sites was found to perform an inner-sphere interaction rather than an outer-sphere interaction on NCNT. The inner-sphere interaction leads to efficient electron transfer and robust PMS adsorption in the presence of organic pollutants, therefore high decontamination efficiency in Fenton-like catalysis. Theoretical calculation, X-ray electron spectrum, X-ray absorption spectrum indicated chemical bonds, specifically ionic bonds, were formed between Mn-N$_4$ moieties and PMS. In contrast, the N-doped surface adsorbed PMS via van der Waals interactions. These findings provide a deep understanding of solid/liquid interface processes and additionally gives a new perspective on the superiority of single atom catalysts.

1. Introduction

Organic micropollutants (OMPs) discharged into aquatic system pose potential threats to ecological security and human health worldwide [1–3]. Heterogeneous Fenton-like catalysis is an increasingly popular remediation technology due to its powerful remediation capacity and few adverse effects [4–9]. Understanding the underlying principles of heterogeneous Fenton-like catalysis is necessary to support the design of new catalysts and the regulation of catalytic oxidation processes [4,10, 11]. Although detailed studies on the active species generated during catalysis have produced important insights [12–16], numerous fundamental questions about interface processes remain unanswered [17–19]. One of the questions is molecular-scale understanding the adsorption and chemical reactivity of solutes at interfaces [20].

Heterogeneous Fenton-like catalysis is a typical solid-liquid interface reaction involving reactant adsorption, surface reaction and product desorption. Tailoring any step results in different kinetics and reaction pathways, thus determining the effectiveness and cost of environmental remediation [11,21]. The interactions between reactants (solutes in water) and solid surface sites necessarily involve multiple molecules and electrostatic forces, influencing binding and interfacial reactivity [20]. Our fundamental knowledge for understanding the physical chemistry of solid/liquid interfaces, in particular their molecular structure and the elementary steps of interfacial reactions, is very limited due to the complexity of the interface structure and molecular interactions [17,20, 22]. To investigate heterogeneous Fenton-like catalysis at solid/liquid interface, ideal solid surface is required to be chemically homogeneous [20]. The rise of single atom catalysts (SACs) may enlighten our understanding of interface processes because of their well-defined active sites and controllable local structure [23,24].

Up to now, SACs are promising in Fenton-like catalysis and the relevant catalysts are mainly limited to carbon-based SACs with metal-N$_x$ moieties [15,23,25–28]. SACs and nitrogen-doped carbon materials are attractive heterogeneous catalysts in Fenton-like catalysis and share similar catalyst design concepts. Both doped N sites and single metal sites (normally transition metal) are isolated atoms in carbon sp^2 networks with a similar geometric effect [29,30]. In other words, single metal atoms on a carbon substrate could be deemed as "doping

heteroatoms" in the graphene structure, that tailors the local structure of the two-dimensional material. Importantly, the atomically-dispersed surface N/metal sites both modulate the electronic state of the carbon framework and act as active sites for oxidants adsorption and activation [31]. Although SACs usually exhibited better peroxymonosulfate (PMS) activation kinetics than their N-doped carbon support [32–34], the underlying mechanism is unclear. A crucial difference between N sites and transition metal sites is that transition metals have numerous d-electrons and empty orbitals that N lacks, which may result in different interfacial bonding behaviors [35]. Therefore, in-depth investigation of the interfacial interaction in the catalytic process may help to provide insights into the interface processes and simultaneously address the origin of superiority of SACs.

In this study, N-doped carbon nanotubes (NCNTs) were utilized as a support to anchor isolated Mn (Mn$_{sa}$-NCNT) for peroxymonosulfate (PMS) activation and OMPs removal. We focused on the interfacial interaction between active sites and reactants at the catalyst/water interface to reveal the effect of interface behavior on decontamination. A comparative study between NCNT and Mn$_{sa}$-NCNT was performed to investigate the origin of superiority of single metal sites in Fenton-like catalysis. Importantly, we propose an interfacial model to understand and predict the interaction between different active sites and reactants in the catalytic oxidation processes, which would facilitate the interpretation of interfacial behavior in multiple heterogeneous remediation processes and inspire novel design of heterogeneous catalysts.

2. Experimental section

2.1. Materials, catalyst preparation and characterizations

Chemicals and reagents are summarized in Text S1. The synthesis details of Mn$_{sa}$-NCNT, Mn$_{np}$-NCNT and NCNT are available in Text S2. The details of characterizations are summarized in Text S3 and Text S4.

2.2. Experimental procedure

For the batch experiments of OMP reaction in an oxidation or adsorption system, a given dose of catalyst was added into 50 mL OMP solution (50 μM). Then different volumes (from 0 to 1 mL) of PMS stock solution (0.1 M) were added into the suspension. Unless otherwise specified, the initial pH of systems was fixed at 3.0 with 0.5 M H$_2$SO$_4$ and 1 M NaOH solution. At predetermined time intervals, 1 mL of the reaction solution was withdrawn and filtered using a 0.5 μm filter membrane. The resulting solution was immediately quenched with 0.5 mL ethanol for further detection. The OMP concentration was measured with ultra-high performance liquid chromatography (UPLC, Wates Co.) with an Agela Venusil C18 column (4.6 × 260 mm, 5 μm). The details about HPLC analysis methods for different OMPs are shown in Table S1.

To determine the PMS adsorption capacity of Mn$_{sa}$-NCNT and NCNT, 5 mg of materials was added into 50 mL deionized water (if needed, add 50 μM 4-CP) or anions solution (NO$_3^-$ and SO$_4^{2-}$). At predetermined time intervals, the suspension was withdrawn and filtered using a 0.5 μm filter membrane. The concentration of residual PMS was analyzed by a chromogenic method using N, N − diethyl−p−phenylenediamine sulfate (NDPDAS) as chromogenic agent. Typically, 0.2 mL sample aliquot was added to a mixed solution (1 mL of 40 mM FeSO$_4$, 0.4 mL of 100 mM NDPDAS, 8.4 mL of deionized water at pH 3.0) and shaken promptly for developing. The absorbance was measured at λ$_{absorption}$= 510 nm using an UV−vis spectrophotometer. The turbidity was detected by a turbidimeter (HACH, America).

The PMS adsorption capacity (q_e) was obtained via a pseudo first order model:

$$\ln(q_e - q_t) = \ln q_e - k_1 t \tag{1}$$

where q_e is adsorption capacity at equilibrium (mmol/g), q_t is adsorbed amount of PMS at time t (mmol/g), and k_1 is the pseudo first order rate constant (min^{-1}). The PMS consumption (denoted as q$_{ep}$) in the presence of 4-CP was approximated with the amount of PMS consumed per unit mass of catalysts at 30 min (mmol/g).

2.3. First principles calculation

We employed the first principles to perform all spin-polarization density functional theory (DFT) calculations within the generalized gradient approximation (GGA) using the Perdew-Burke-Ernzerhof (PBE) formulation [36–38]. The projected augmented wave (PAW) potentials were selected to define the ionic cores [39]. Valence electrons were described by using a plane wave basis set with a kinetic energy cutoff of 450 eV. Partial occupancies of the Kohn−Sham orbitals were allowed using the Gaussian smearing method and a width of 0.05 eV. The electronic energy was considered self-consistent when the energy change was smaller than 10^{-5} eV. If the energy change was less than 0.02 eV•Å^{-1}, the geometry optimization was considered convergent. A vacuum layer of 15 Å was usually added to the surface to minimize artificial interactions between periodic images. Spin polarized calculations were performed for this calculation. The weak interaction was described by DFT+D3 method using empirical correction in Grimme's scheme [40]. Finally, the adsorption energies (E_{ads}) were calculated as:

$$E_{ads} = E_{ad/sub} - E_{ad} - E_{sub} \tag{2}$$

where $E_{ad/sub}$, E_{ad} and E_{sub} are the total energies of the optimized PMS/substrate system, the PMS and the clean substrate, respectively.

The charge density difference ($\Delta\rho$) was calculated as:

$$\Delta\rho = \rho_{ad/sub} - \rho_{ad} - \rho_{sub} \tag{3}$$

where $\rho_{ad/sub}$, ρ_{ad} and ρ_{sub} is the charge density of optimized PMS/substrate system, the PMS and the clean substrate, respectively.

The density overlap region indicator (DORI) was defined according to reported methods[41], which can be seen as follows. First, we define a dimensionless quantity θ as:

$$\theta(\mathbf{r}) = \frac{\left(\nabla \mathbf{k}^2(\mathbf{r})\right)^2}{\left(\mathbf{k}^2(\mathbf{r})\right)^3} = \frac{\left(\nabla\left(\frac{\nabla\rho(\mathbf{r})}{\rho(\mathbf{r})}\right)^2\right)^2}{\left(\frac{\nabla\rho(\mathbf{r})}{\rho(\mathbf{r})}\right)^6} \tag{4}$$

where $\mathbf{k}(\mathbf{r})$ is the local momentum vector, defined as:

$$\mathbf{k}(\mathbf{r}) = \frac{\nabla\rho(\mathbf{r})}{\rho(\mathbf{r})} \tag{5}$$

where $\rho(\mathbf{r})$ is electron density in real space, $\nabla\rho(\mathbf{r})$ is the electron density gradient in real space. The DORI could be defined as:

$$DORI = \frac{\theta}{1 + \theta} \tag{6}$$

3. Results and discussion

3.1. Atomic structure and chemical state analysis

The synthesis scheme of NCNT and Mn$_{sa}$-NCNT is shown in Fig. 1a. The NCNT was synthesized via doping N into the CNT sp^2 framework with melamine and 1,10-phenanthroline as N-containing precursors. The isolated Mn sites were introduced by assembling 1,10-phenanthroline-coordinated Mn onto NCNT surface and annealing at 600 °C. As a control, we also synthesized NCNT with attached Mn nanoparticles (Mn$_{np}$-NCNT). No obvious agglomerates of Mn nanoparticles could be observed in the scanning electron microscope (SEM) images (Fig. S1) and transmission electron microscope (TEM) images (Fig. S2) of Mn$_{sa}$-NCNT. X-ray diffraction (XRD) patterns of the catalysts are illustrated in
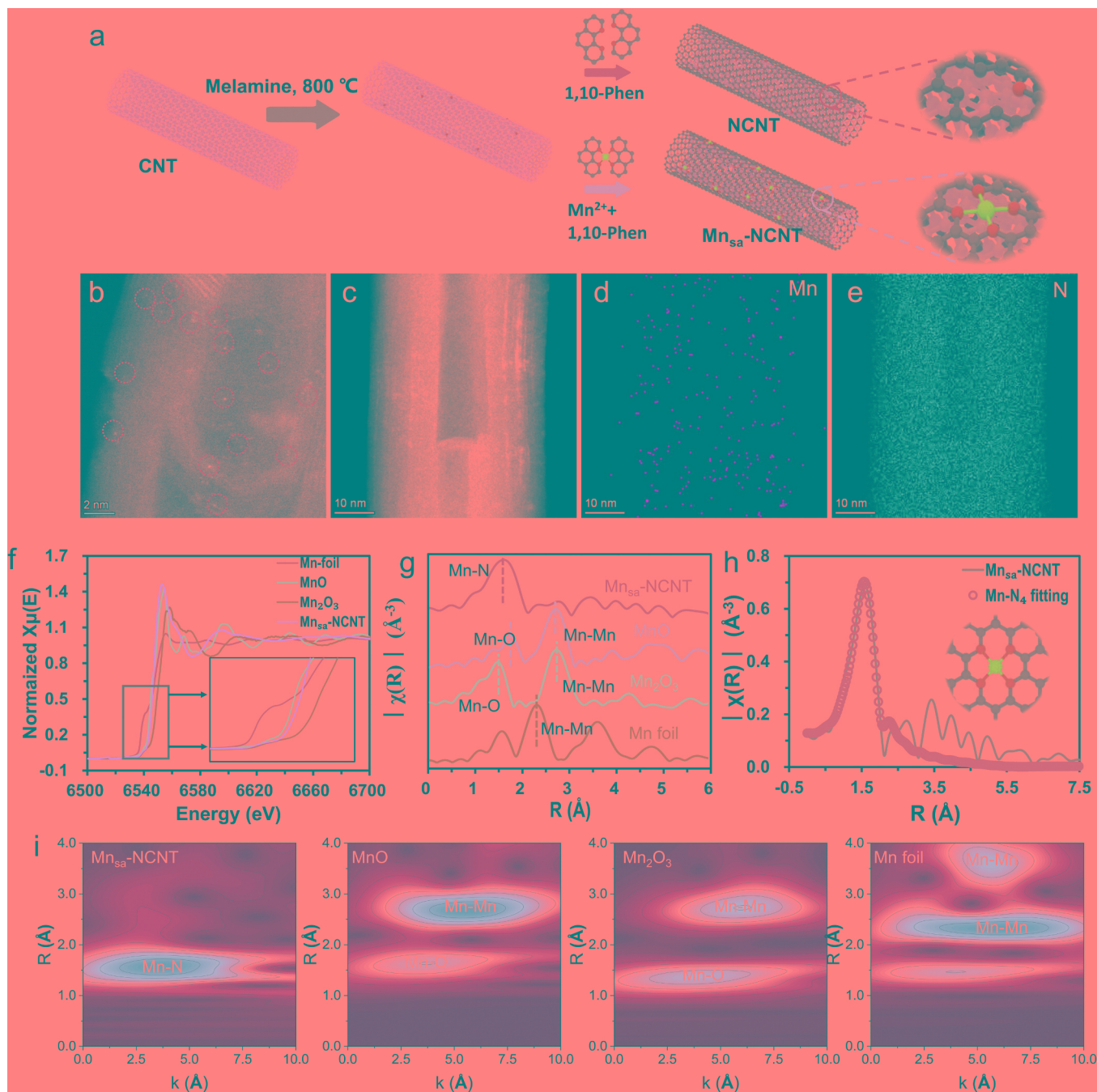
Fig. 1. Synthetic illustration and morphology characterizations. (a) Schematic illustration of the preparation strategy. (b) Atomic-resolution HAADF-STEM image of Mn_{sa}-NCNT. (**c**) HAADF-STEM images of Mn_{sa}-NCNT and the corresponding EDS mapping of (d) Mn sites and (e) N sites. (f) Mn k-edge XANES of Mn_{sa}-NCNT and reference samples. (g) FT of the k^2-wieghted EXAFS of different samples. (h) Corresponding EXAFS fitting plots of Mn_{sa}-NCNT, inset: the proposed $Mn-N_4$ architectures. (i) WT-EXAFS of Mn_{sa}-NCNT, MnO, Mn_2O_3 and Mn foil, respectively.

Fig. S3. No characteristic crystal peaks of Mn are seen in Mn_{sa}-NCNT diffraction pattern, further precluding the presence of any large crystalline particles containing manganese. The aberration-corrected high-angle dark-field scanning TEM was carried out to characterize the dispersion of Mn species on Mn_{sa}-NCNT. The single bright dots in Fig. 1b correspond to atomically-dispersed Mn, which could be obviously distinguished from the N-doped carbon substrate. The corresponding EDS mapping further demonstrates the homogeneous distribution of Mn and N over the whole architecture (Fig. 1c-e). All the aforementioned results indicate that the isolated Mn has been successfully incorporated into the N-doped carbon sp^2 framework.

Synchrotron-based X-ray absorption near-edge structure (XANES)

and extended X-ray absorption fine structure (EXAFS) spectroscopy were employed to elucidate the chemical states and detailed structural information of the isolated Mn sites. The energy absorption threshold (Fig. 1 f) of Mn_{sa}-NCNT located between that of MnO and Mn_2O_3, suggesting that the valence of Mn atoms in Mn_{sa}-NCNT is situated between Mn^{2+} and Mn^{3+} [42]. Fig. 1g shows the Fourier transform (FT) EXAFS for the Mn_{sa}-NCNT compared with several reference samples. The absence of the Mn-Mn scattering path indicates that isolated Mn atoms have distributed over the carbon sp^2 framework. Mn_{sa}-NCNT displays a major scattering path at around 1.60 Å corresponding to Mn-N bonding rather than the Mn-O scattering paths at length around 1.5 or 1.75 Å. Accurate coordination configuration was obtained by EXAFS fitting

(Fig. 1h and Table S2). The fitting FT-EXAFS uncovers a main peak derived from Mn–N first shell coordination with a coordination number of 4 and average bond length of 2.11 Å. Since the X-ray photon spectroscopy (XPS) reveals a high proportion of pyridinic N in Mn_{sa}-NCNT (Fig. S4), the coordination structure is proposed as the Mn-N₄ architecture, as shown in the inset of Fig. 1h. The wavelet transform (WT) plots of Mn samples reveal that an intensity maximum corresponding to Mn-Mn is observed in MnO, Mn_2O_3 and Mn foil rather than in Mn_{sa}-NCNT (Fig. 1i), further indicating the presence of isolated Mn coordinated to N on the NCNT surface [43].

The physicochemical properties of multiple catalysts were further characterized. CNT, NCNT, Mn_{np}-NCNT and Mn_{sa}-NCNT all exhibit one peak at approximately 26° indexed to the (002) crystal face of graphitic carbon (Fig. S3) [44]. The peaks of Mn_{np}-NCNT at 35° and 41° are assigned to reflections of the (110) and (200) crystal planes of manganosite (JCPDS#07–0230), corresponding to the observed nanoparticles in the TEM images of Mn_{np}-NCNT (Fig. S2a-c). Raman spectra reveal the calculated I_D/I_G values of CNT, NCNT and Mn_{sa}-NCNT are 0.224, 0.315 and 0.296 (Fig. S5), respectively. NCNT exhibits slightly

larger I_D/I_G values than Mn_{sa}-NCNT, indicating the formation of more defects and disordered structures in the NCNT. Importantly, the doping of pyridinic N in pristine sp^2 carbon framework usually requires simultaneous construction of surface defects to avoid the formation of graphite N [45]. N 1 s XPS spectra of NCNT and Mn_{sa}-NCNT exhibit three characteristic peaks assigned to pyridinic N, pyrrolic N and graphitic N (Fig. S4), respectively. The high proportion of pyridinic N in the N species primarily contributes the defects and Mn-coordination environment. Besides, the anchoring of Mn in Mn_{sa}-NCNT promoted N doping (Table S4), which ensures atomic-level dispersion of the metal on the carbon surface. Aforementioned results show that the primary active sites in NCNT and Mn_{sa}-NCNT are inferred to be the doped N and Mn-N₄ sites, respectively.

3.2. Activity of Fenton-like catalysis and dominated activation mechanism on different active sites

To assess the effect of active sites of different catalysts on PMS activation activity, the Fenton-like catalytic performance was evaluated
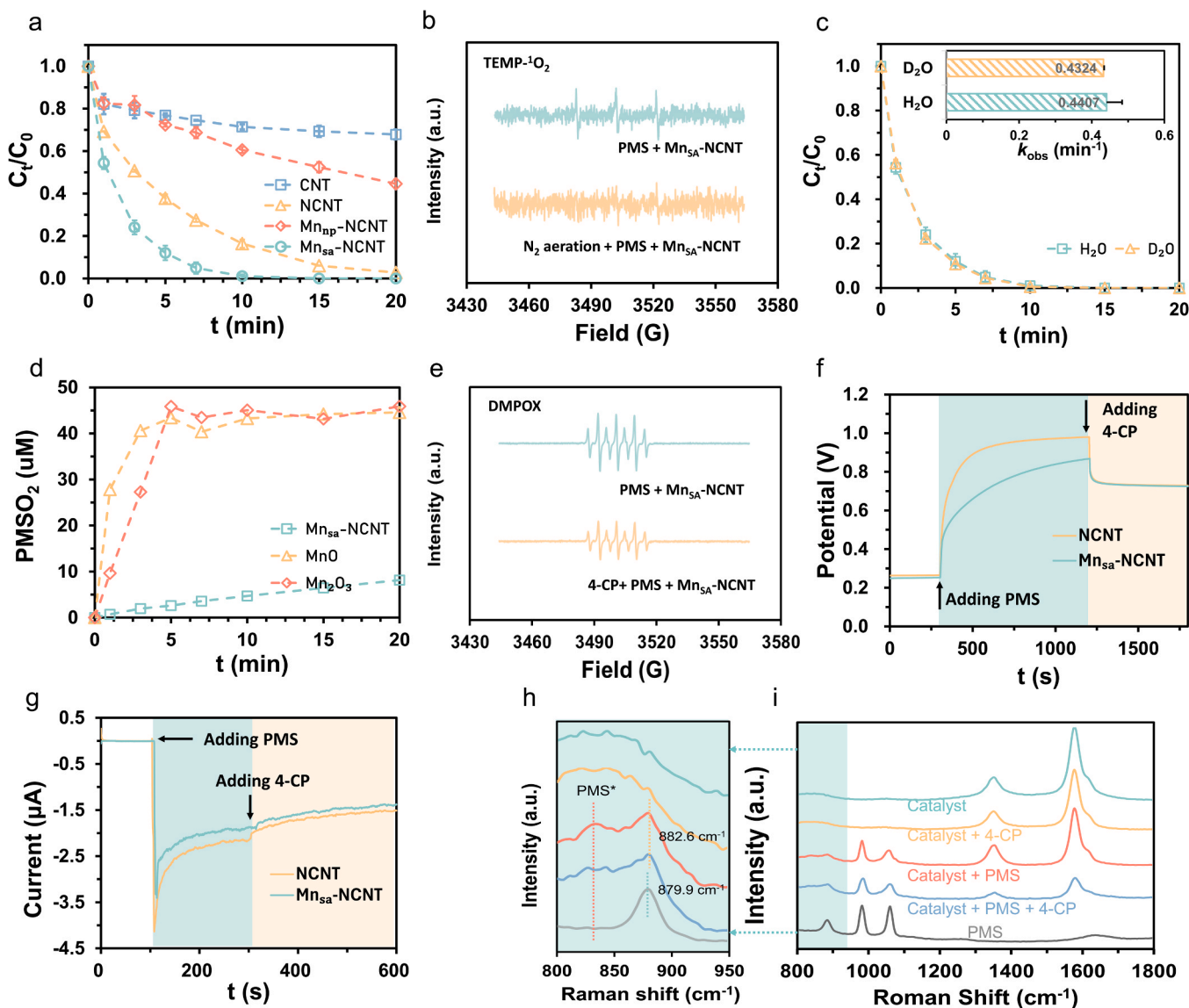

Fig. 2. Removal kinetics and reaction mechanism. (**a**) Degradation kinetics for 4-CP removal by PMS activation with different catalysts. (**b**) The ESR spectrum of $^1O_2$ in Mn_{sa}-NCNT/PMS system. (**c**) 4-CP removal kinetics of the Mn_{sa}-NCNT/PMS system in H_2O/D_2O. (**d**) $PMSO_2$ generation kinetics in Mn based catalyst/PMS systems. (**e**) DMPOX (5,5dimethyl-2-pyrrolidone-N-oxyl) generated in the Mn_{sa}-NCNT/PMS/DMPO system. (**f**) Chronoamperometry for reaction analysis. (**g**) i-t curve for reaction analysis. (**h-i**) The in-situ Raman spectra of different systems. Reaction conditions: Catalyst: 0.1 g/L, 298 K, PMSO: 50 μM, pH 3, PMS: 1 mM, 4-CP: 50 μM.

via 4-chlorophenol (4–CP) removal. As shown in Fig. 2a, the CNT/PMS system shows a minimal removal of 4-CP in 20 min. NCNT activates PMS to rapidly degrade 100% 4-CP in 20 min because the incorporation of N into the sp^2 carbon framework disturbs the surface electronic structure which enhances PMS adsorption [46]. Solo PMS or Ma$_{sa}$-NCNT only exhibit 3% or 21% 4-CP removal (Fig. S7). However, the Mn$_{sa}$-NCNT/PMS system achieves complete removal of 4-CP in 10 min with k_{obs} of 0.4407 min^{-1}, which is much higher than Mn$_{np}$-NCNT because of the maximum utilization of metal atoms in SACs (Fig. S8). It is noted that the Mn$_{sa}$-NCNT/PMS system shows a much better performance for 4-CP removal than its homogeneous counterpart (Mn^{2+}/PMS) or heterogeneous manganese oxides (MnO & Mn$_2$O$_3$) (Fig. S9). The Mn$_{sa}$-NCNT also exhibits high and stable degradation performance in a wide pH of 3–11 (Fig. S10). All the aforementioned results show the superiority of Mn-N$_4$ sites on the sp^2 carbon framework as compared with doped N, Mn nanoparticles and manganite.

The mechanism of 4-CP removal was further investigated using quenching studies to identify the reactive species. Ethyl alcohol (EtOH) and tert-butyl alcohol (TBA) did not inhibit the removal of 4-CP (Fig. S11), and the characteristic peaks of OH$^{\bullet}$ and SO$_4^{\bullet-}$ were absent in the PMS/Mn$_{sa}$-NCNT/DMPO system (Fig. 2e), thus excluding the contribution of OH$^{\bullet}$ and SO$_4^{\bullet-}$. Furfuryl alcohol (FFA) inhibits decontamination, suggesting the possible involvement of ^{1}O$_2$. However, FFA acts as an inhibitor in the NCNT/PMS system (classical mediated electron transfer (MET) processes) which cannot produce ^{1}O$_2$ (Fig. S12) [47]. Previous studies have suggested that FFA may be degraded in MET system, thus misleading the contribution of ^{1}O$_2$ [47,48]. Due to the limitations of FFA as an indicator of ^{1}O$_2$, electron paramagnetic resonance (EPR) spectra were obtained to investigate the role of ^{1}O$_2$ (Fig. 2b). The weak three-line spectrum of the TEMP-^{1}O$_2$ adduct in the Mn$_{sa}$-NCNT/PMS system suggested the negligible role of ^{1}O$_2$. Besides, the peaks of TEMP-^{1}O$_2$ are reported to be formed via deprotonation of TEMP (to generate TEMP$^{+\bullet}$) and O$_2$ addition of TEMP$^{+\bullet}$ in MET systems [47,49]. Therefore, the disappearance of the characteristic peaks of ^{1}O$_2$ after N$_2$ aeration in the Mn$_{sa}$-NCNT/PMS system further excludes the involvement of ^{1}O$_2$ [49]. The longevity of singlet oxygen (^{1}O$_2$) in deuterated water (D$_2$O) surpasses that observed in regular water (H$_2$O). However, in D$_2$O solution, both the removal efficiency and the rate constant (k_{obs}) of the Mn$_{sa}$-NCNT/PMS system exhibit negligible alteration (Fig. 2c). This observation excludes the participation of ^{1}O$_2$ in the removal of 4-chlorophenol (4-CP). Then, the high-valent manganese species become candidates responsible for decontamination. The characteristic conversion from PMSO to PMSO$_2$ in high-valent metal-based processes is observed in the Mn$_{sa}$-NCNT/PMS system (Fig. S13) [13]. However, the produced high-valent Mn (~8 μM) cannot satisfy the stoichiometric equilibrium of the oxidation process, as the oxidation of 50 μM of contaminant requires at least 50 μM of high-valent Mn. Moreover, if the dominant reactive species of the Mn$_{sa}$-NCNT/PMS system are high-valent Mn, then more PMSO$_2$ should be produced than in the MnO/PMS or Mn$_2$O$_3$/PMS systems because Mn$_{sa}$-NCNT exhibit better performance of 4-CP removal efficency. However, the MnO/PMS and Mn$_2$O$_3$/PMS systems produce more PMSO$_2$ (~45 μM in 5 min, Fig. 2d). These results indicate the negligible contribution of high-valent Mn. The above results also rule out the possibility of PMS decomposition induced by the generation of radicals and high-valent Mn.

Finally, the characteristic signals of DMPOX (5,5-dimethyl-2-pyrrolidone-N-oxyl, the direct oxidation products of DMPO) in the EPR spectra (Fig. 2e) suggest that electron transfer processes (ETPs) may dominate the degradation. Electrochemical analysis was used to identify the ETP regime. Fig. 2f shows that the addition of PMS leads to an increase in potential due to the PMS-catalyst complex (PMS*) formed on the surface. After the addition of 4-CP, the PMS* decomposed to oxidize the contaminants, resulting in a decrease in potential. The i-t curve shows the oxidation current formed after the addition of PMS and 4-CP (Fig. 2g). Besides, the observed PMS* peak (reactive complex in mediated electron transfer processes) in in-situ Raman spectra (Fig. 2h-i) also

demonstrate that the mediated electron transfer processes dominate the decontamination mechanism [14,47].

3.3. PMS utilization kinetics on different active sites

Due to the similar geometric effect and high activity of N and Mn-N$_4$ sites, we selected NCNT and Mn$_{sa}$-NCNT to further investigate the PMS adsorption kinetics and interaction behavior between active sites and PMS molecules, to obtain insights into the interface dynamics and the superiority of SACs. Fig. S14-S15 show that Mn$_{sa}$-NCNT exhibits significantly higher k_{obs} than NCNT for multiple OMPs including phenol (PE), bisphenol A (BPA), p-hydroxybenzoic acid (PHBA), p-nitrophenol (PNPE) and o-phenylphenol (OPP).

Previous studies have proven a positive correlation between the PMS adsorption capacity and catalytic performance of catalyst [48,50,51]. However, according to the PMS adsorption capacity (q_e) of the different catalysts (Fig. S16), NCNT exhibits an obviously higher q_e than Mn$_{sa}$-NCNT, which is inconsistent with the pollutant degradation performance. In a series of experiments using different initial PMS dosages (C$_{PMS, Initial}$: 0.1 ~ 2.0 mM), NCNT also exhibits a higher PMS adsorption capacity than Mn$_{sa}$-NCNT (Fig. 3a). The k_{obs} values for 4-CP removal of NCNT are inferior to that of Mn$_{sa}$-NCNT at different C$_{PMS, Initial}$ (Fig. 2b). The above anomalies suggest that the PMS adsorption capacity of the catalyst alone fails to accurately describe the activity of the catalyst, and thus we question why Mn-N$_4$ sites have higher activity than the N sites, even though the q_e is lower. Moreover, we found a positive linear relationship (R^2 = 0.9857 for NCNT and R^2 = 0.9179 for Mn$_{sa}$-NCNT, Fig. 3b) between k_{obs} and C$_{PMS, Initial}$ at low PMS loading from 0.1 to 0.5 mM. However, the oxidation capacity of both catalysts is not sensitive to PMS loading at higher initial PMS dosages from 1.0 to 2.0 mM (Fig. 3b), suggesting both catalysts reach a limit for PMS utilization [52], even q_e continues to increase.

For a deep understanding of these phenomena, we further investigated the catalytic process from the perspective of interface interaction. At the solid-liquid interface, chemicals including PMS, pollutants and oxidation intermediates are adsorbed on the catalyst surface. Both PMS and contaminant molecules compete for the active sites with a consequent reduction in PMS utilization capacity. The adsorption of OMPs depends on the hydrophobicity of the surface. No obvious change is observed in the hydrophobicity of the materials after the incorporation of atomically-dispersed Mn (Fig. S17), so the adsorption capacities of NCNT and Mn$_{sa}$-NCNT for various pollutants are similar (Fig. S18). The PMS consumption in the presence of 4-CP (adsorption and decomposition of PMS, which was denoted as q_{ep}) was determined (Fig. 3c-d). It appears that the utilization of PMS by NCNT is inhibited in the presence of 4-CP. The difference between q_e and q_{ep} gradually increases from 0.04 to 9.72 mmol/g as the C$_{PMS, Initial}$ increases from 0.1 to 2.0 mM (Fig. 3c and S19a), indicating strong competition between PMS and the organic pollutants on the NCNT surface. However, Fig. 3d shows that the presence of 4-CP slightly intensifies the PMS utilization of Mn$_{sa}$-NCNT at low C$_{PMS, Initial}$ (0.1 and 0.25 mM). The inhibition of PMS utilization at high C$_{PMS, Initial}$ (0.5–2 mM) is observed (Fig. S19b), but is obviously smaller compared to NCNT. Importantly, the q_{ep} of Mn$_{sa}$-NCNT is higher than that of NCNT at all C$_{PMS, Initial}$, which is in agreement with its degradation performance (Fig. 3b). Our results suggest that PMS adsorption on Mn$_{sa}$-NCNT is robust in comparison with NCNT. Thus, Mn$_{sa}$-NCNT has more favorable PMS utilization and degradation performance in the presence of organics.

Besides, the q_{ep} rather than q_e show a similar variation trend to k_{obs} (Fig. S19 and Fig. 3b). Both q_{ep} and k_{obs} reach a maximum around 1 mM PMS and remain stable as the C$_{PMS, Initial}$ increases from 1.0 to 2.0 mM. As illustrated in Figs. 3e-3f, a better linear correlation is established between q_{ep} and k_{obs} rather than between q_e and k_{obs} in both NCNT and Mn$_{sa}$-NCNT with R^2 of 0.9861 and 0.9120, respectively. This demonstrates that PMS consumption (when organics are present) rather than PMS adsorption capacity could accurately indicate the catalytic
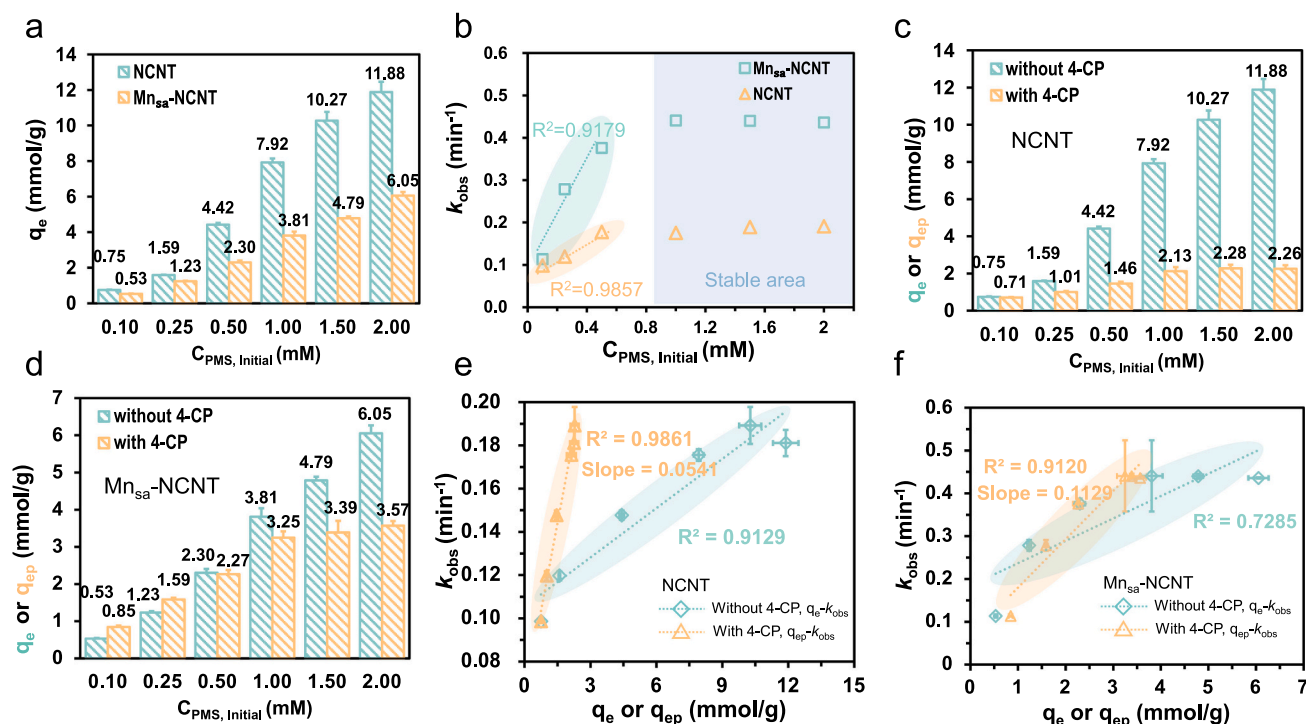
Fig. 3. Kinetics studies on Fenton-like catalysis and PMS adsorption. (**a**) PMS adsorption capacity of NCNT and Mn_{sa}-NCNT at different initial PMS dosage. (**b**) Relationship between k_{obs} and initial PMS dosages. PMS consumption of (**c**) NCNT and (**d**) Mn_{sa}-NCNT in the absence/presence of 4-CP. Reaction conditions Correlation analysis between kobs and q_e in (**e**) NCNT/PMS and (**f**) Mn_{sa}-NCNT/PMS systems. Reaction conditions if not specified: OMPs: 50 μM, PMS: 1.0 mM, Mn_{sa}-NCNT: 0.1 g/L, 298 K, pH 3.0.

performance of the different materials, and that consideration of the co-existence of substances in the interfacial reaction is necessary for a deep understanding of the catalytic processes. The presence of organic compounds disrupts the utilization of peroxymonosulfate (PMS), resulting in a limitation of PMS utilization by the catalyst at a PMS loading concentration of 1 mM, as illustrated in Fig. 3e-f. With an initial increase in PMS concentration to 2 mM, the removal efficiency of pollutants also reaches a saturation point, remaining stable within the PMS loading range of 1 to 2 mM.

After analyzing the above experimental results, we propose a

theoretical interfacial model to explain the robustness of PMS adsorption on single-atom catalysts in the presence of OMPs. According to the strength of the interaction of the catalyst surface with reactants (PMS and organics in water), the interaction behaviors at the solid/liquid interface could be categorized into inner-sphere and outer-sphere interactions [53]. The outer-sphere interaction is based on intermolecular forces and involves a longer intermolecular distance, resulting in weak interaction strength. In contrast, inner-sphere interactions based on chemical bonding induce stronger adsorption of reactants onto the activator surface. Moreover, the adsorption based on outer-sphere
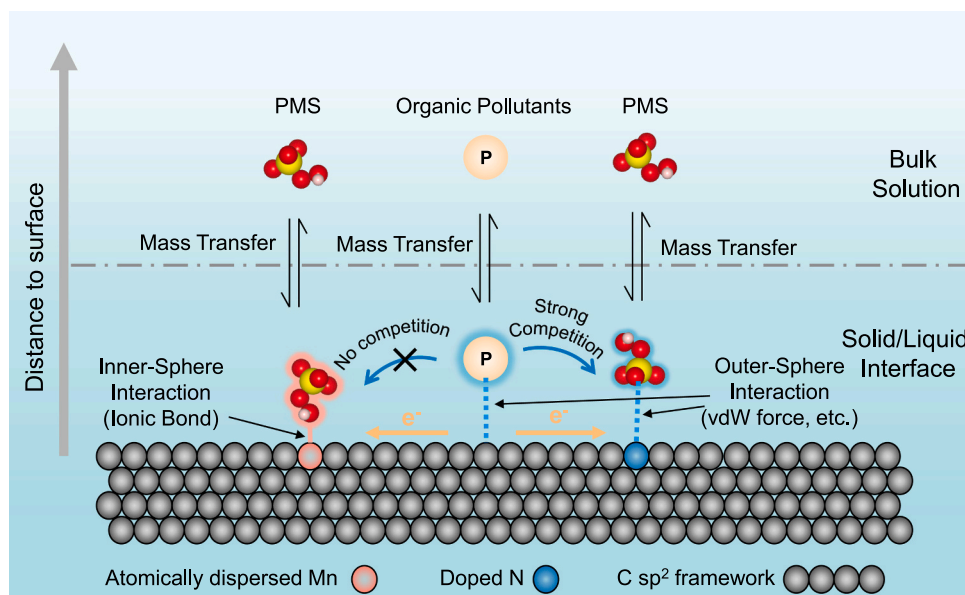

Fig. 4. The diagram of proposed interfacial interaction model.

interactions involves reversible multilayer adsorption but the adsorption based on inner-sphere interactions involves irreversible monolayer adsorption. The adsorption of PMS and organics on NCNT is a consequence of van der Waals (vdW) forces, π-π stacking and hydrophobic interaction, which are outer-sphere interaction (Fig. 4) [54,55]. Competition between outer-sphere interactions would weaken PMS utilization on NCNT. For Mn_{sa}-NCNT, the organics adsorption is also derived from outer-sphere interaction, but PMS adsorption on Mn-N$_4$ sites is based on inner-sphere interaction by virtue of the unsaturated coordination active sites and the chemically active peroxide bond [23, 56,57]. The strong interaction between PMS and Mn-N$_4$ exhibits excellent robustness against disruptions from outer-sphere interaction. Besides, the slope of the q_e vs k_{obs} line for the Mn_{sa}-NCNT/PMS/4-CP

(0.1129, Fig. 3e) system is greater than that of NCNT/PMS/4-CP system (0.0541, Fig. 3f) because the inner-sphere electron transfer accompanied with inner-sphere interaction exhibits higher efficiency [58]. As a result, Mn_{sa}-NCNT enhances the utilization of PMS and achieves better oxidation performance.

3.4. Evidence for interaction model at solid-liquid interface

To verify the proposed theoretical model (Fig. 4), the effect of other outer-sphere interactions on PMS utilization at the solid-liquid interface was investigated. Anions as those chemically inert in Fenton-like catalysis (SO_4^{2-} and NO_3^-) were introduced into the catalyst/PMS systems as competing ions with HSO_5^- in outer-sphere interactions (Figs. 5a-
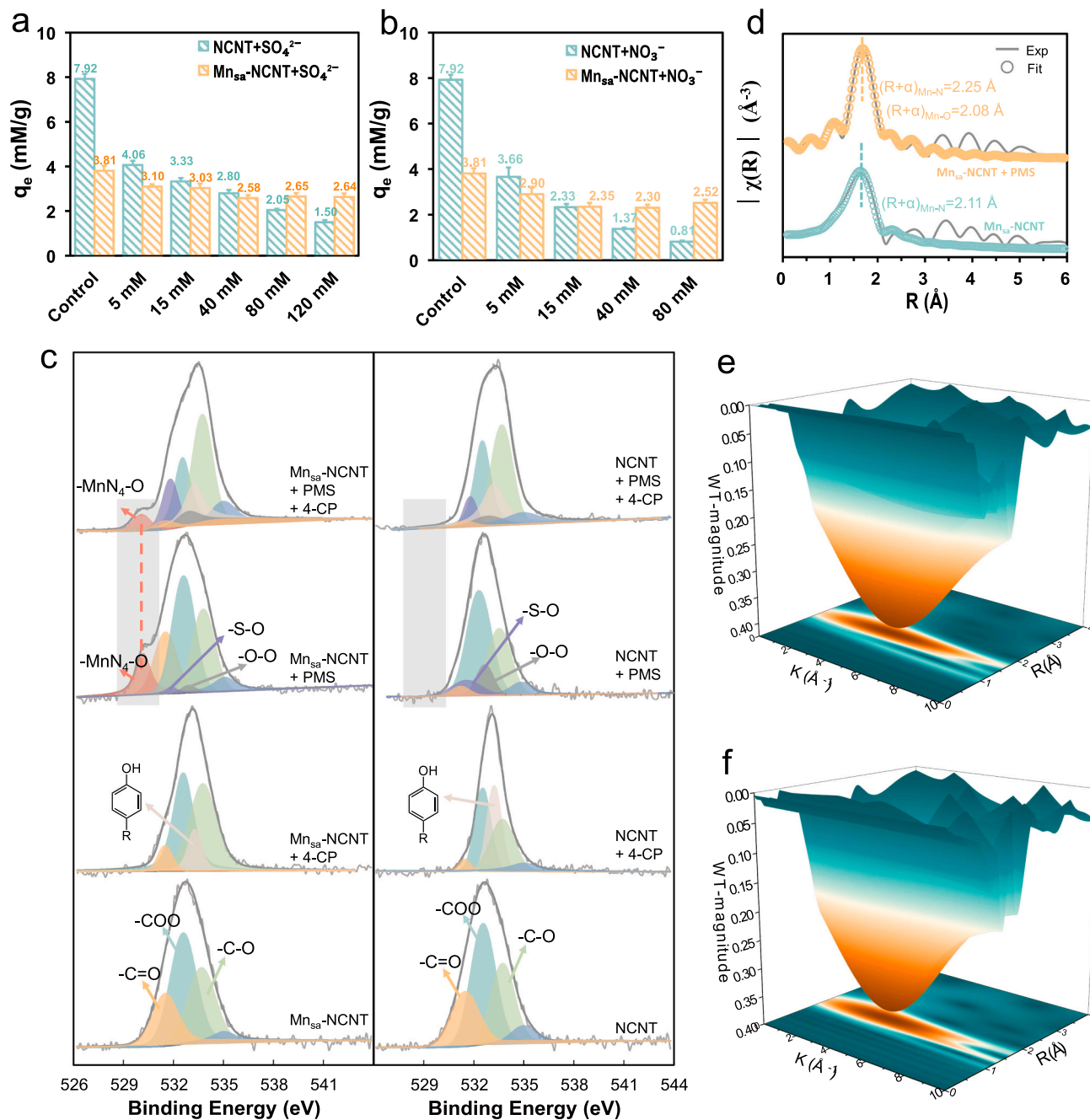

Fig. 5. Verification of interfacial interaction. Effect of (**a**) SO_4^{2-} and (**b**) NO_3^- on PMS adsorption by NCNT and Mn_{sa}-NCNT. (**c**) XPS O 1 s spectra of different materials. (**d**) FT-EXAFS of Mn_{sa}-NCNT before and after PMS adsorption. WT-EXAFS of Mn_{sa}-NCNT before (**e**) and after (**f**) PMS adsorption. Reaction conditions if not specified: OMPs: 50 μM, PMS: 1.0 mM, Mn_{sa}-NCNT: 0.1 g/L, 298 K, pH 3.0.

5b). Notably, the inhibition of PMS utilization of NCNT by sulfate increases significantly with sulfate concentration. A similar inhibition trend could also be observed when NO_3^- was added into the NCNT/PMS system. The competitive interaction based on the outer-sphere interaction (van der Waals forces or electrostatic interaction) for active sites on the NCNT surface is responsible for the strong inhibition. However, the PMS adsorption by Mn_{sa}-NCNT is slightly restrained and gradually stabilized at 2.5 mmol/g as more anions are added, also indicating the robustness of the interaction between Mn-N_4 sites with HSO_5^-. The reduction in q_e occurs because Mn_{sa}-NCNT surface has a certain number of N/C sites available to adsorb the PMS. The above results further demonstrate the possible inner-sphere interaction between Mn-N_4 sites and PMS molecules.

The cornerstone of inner-sphere interaction is chemical bonding, which involves a rearrangement of electron orbitals and a shorter interaction length. The XPS was applied to investigate the alteration in the chemical microenvironment due to the possible chemical bonding. XPS O 1 s spectra of NCNT and Mn_{sa}-NCNT in different systems are illustrated in Fig. 5c. The pristine NCNT and Mn_{sa}-NCNT manifest three O species assigned to -C=O, -COO and -CO species. After 4-CP adsorption, a peak at 533.2 eV assigned to phenolic hydroxyl group (Fig. S20a) is observed in both NCNT and Mn_{sa}-NCNT (Fig. 5c), and no obvious peak shift of phenolic hydroxyl group is detected. These indicate that 4-CP adsorption on NCNT and Mnsa-NCNT belongs to outer-sphere interaction because chemical bonds fail to form or break in the processes. Curiously, a new peak appears at 530.0 eV in the O 1 s spectra of Mn_{sa}-NCNT but not in that of NCNT after PMS adsorption. This new peak shifts toward low binding energy as compared with the S-O and O-O species in PMS (Fig. S20b), indicating considerable variation in the electronic structure of the O in PMS due to the chemical bonding between electropositive Mn-N_4 sites and PMS [59]. These spectra give clear evidence that an inner-sphere interaction occurs when Mn_{sa}-NCNT adsorbs PMS and the outer-sphere interaction dominate the PMS utilization by NCNT. After the oxidation reaction, O-MnN_4 specie declines obviously due to decomposition and desorption after the Fenton-like catalysis (Fig. 4c and Fig. S21a). For NCNT, the O-O species responsible for oxidation diminishes after reaction (Fig. S21b). All the results further support the inner-sphere interaction between Mn-N_4 sites and PMS, and the outer-sphere interaction for other adsorption and reaction processes.

Coordination microenvironment and interaction distance were accurately investigated via XAS for further insights into inner-sphere interaction. As depicted in the XANES spectra (Fig. S22), the adsorption edge displaces toward high energy due to the elevation of valence state, indicating that Mn sites donate electrons to PMS when they chemically bond with PMS. This facilitates efficient inner sphere electron transfer, which is consistent with the results of PMS utilization. According to the FT-EXAFS spectra (Fig. 5d), the main peak of Mn_{sa}-NCNT shifts to longer scattering length after adsorbing PMS, indicating that the local coordination structure of Mn_{sa}-NCNT is changed. The first shell peak in FT-EXAFS of Mn_{sa}-NCNT with PMS adsorbed (Fig. S23) is fitted to the scattering of Mn-N and Mn-O with coordination number of 4 and 1, respectively (Table S5). The Mn-O path of 2.08 Å solidly demonstrate the inner-sphere interaction between Mn-N_4 and PMS molecules because the length of 2.08 Å has achieved bonding length. Strong binding between Mn and O could also alter the Mn-N scattering length from 2.11 to 2.25 Å. Wavelet-transform (WT) EXAFS could offer high resolution in both k and R space to further discriminate the difference before and after PMS adsorption. Fig. 5e and Fig. 5f indicate that the Mn_{sa}-NCNT with PMS adsorption exhibited one maximum peak at around 4.08 Å^{-1} and 1.59 Å, which is slightly different from that of pristine Mn_{sa}-NCNT at around 3.84 Å^{-1} and 1.56 Å. The spectra show that changes occur in the coordination environment of Mn after PMS adsorption. The shift towards high wavenumbers after PMS adsorption could be attributed to change of bonding of Mn from N to O, which has a higher atomic number [43].

3.5. The theoretical study of interface interaction

Having obtained solid evidence for the proposed interaction model, theoretical calculations were performed to investigate site-PMS interaction at the atomic level. Possible interaction configurations of PMS with NCNT and Mn_{sa}-NCNT are proposed as schematically described in Fig. S24 and Fig. 6a-e according to the categories of O atoms in PMS molecule. FT-EXAFS shows the Mn-O coordination number is 1, thus, the adsorption models of Mn_{sa}-NCNT were simulated for Pauling type (end-on type) configurations. As pictured in Figs. 6a-6b and Fig. S25-S26, the N-doped carbon surface exhibits two interaction configurations for PMS adsorption with E_{ads} of − 1.730 eV and − 1.646 eV. The shortest distances between N and O are 3.28 Å and 3.43 Å for -SO_3 type and -OOH type configurations, respectively, which are far beyond bonding length (almost 1.5 Å). However, the lengths of Mn-O in O_α-Pauling type, O_β-Pauling type and O_γ-Pauling type configurations are 2.02, 2.10 and 2.15 Å (Figs. 6c-6e and Fig. S27-S29), respectively. Due to the large atomic radius of Mn, its bonding distance to O is around 2.1 Å. The optimized Mn-O bond lengths are in bonding distance, further indicating the inner-sphere interaction between PMS and Mn-N_4 sites. In addition, inner-sphere interactions in the O_α-Pauling type, O_β-Pauling type and O_γ-Pauling type result in higher E_{ads} (3.063, 2.817 and 2.746 eV), which favors stronger adsorption bonding and protection from outer-sphere interactions.

The density overlap regions indicator (DORI) provides a topological classification that enables simultaneous visualization of both bonding patterns and nonbonding interactions [41]. With this powerful tool, we can clearly distinguish the dominant interactions between the active sites and PMS when selecting the –SO_3 type and O_α-Pauling type as primary interaction configurations. As shown in Fig. 6f and Fig. S30-S31, an obvious region of vdW interaction rather than bonding interaction could be observed between the PMS molecule and NCNT surface. For Mn_{sa}-NCNT (Fig. 6g and Fig. S32), a region corresponding to chemical bonding interaction is observed between O_α and Mn (similar to the region between Mn and N). These results solidly demonstrate the inner-sphere interaction between Mn-N_4 sites and PMS molecules. Besides, electronic localization function (ELF) is applied to describe the degree of localization of electrons and decipher the nature of Mn-O bonding. Fig. 6h shows strong electron localization in the C-N and C-C interaction due to the covalent character of paired electrons in the C-N and C-C bond. However, no significant electron localization could be seen between the N and O atoms (or between C and O) because the vdW interactions do not require shared electrons (Fig. S33). For Mn and O_α at the interface, overlap of charge density is observed (Fig. S33) but the valence electrons of Mn are highly delocalized (Fig. 6i). These results indicate that the Mn-O bond is an ionic bond.

The 4-CP-site interactions were investigated at the atomic level to further elucidate the interfacial processes. In addition to Mn-N_4 and pyridinic N, carbon vacancy and sp^2 framework (Fig. S34) were also considered as the functional sites for 4-CP adsorption due to potential π-π interactions. As shown in Fig. S35a-d and Figs. S36-S39, 4-CP adsorption on Mn-N_4 site has slightly higher E_{ads} of 0.661 eV than that on N site (0.556 eV), C vacancy (0.5224 eV) and carbon sp^2 framework (0.551 eV). The shortest distances between the material surface and 4-CP (Fig. S38) are all beyond the bonding distance. The DORI analysis (Fig. S35 and S40-S43) shows that vdW interaction and π-π interaction dominantly contribute to the intermolecular interactions and no chemical bonds are formed. All these data confirm that the 4CP is adsorbed on the Mn_{sa}-NCNT and NCNT surface via outer-sphere interactions. Therefore, the reasons for robust PMS adsorption on Mn_{sa}-NCNT could be summarized as follows: 1) The energy difference between PMS adsorption and 4-CP adsorption on Mn-N_4 site is obviously higher than that on N site (Fig. 6j), thus PMS adsorbed on Mn-N_4 site is more stable; 2) the adsorption of PMS on Mn-N_4 based on inner-sphere interaction is chemisorption (ionic bond), thus PMS adsorption on Mn-N_4 site is irreversible.
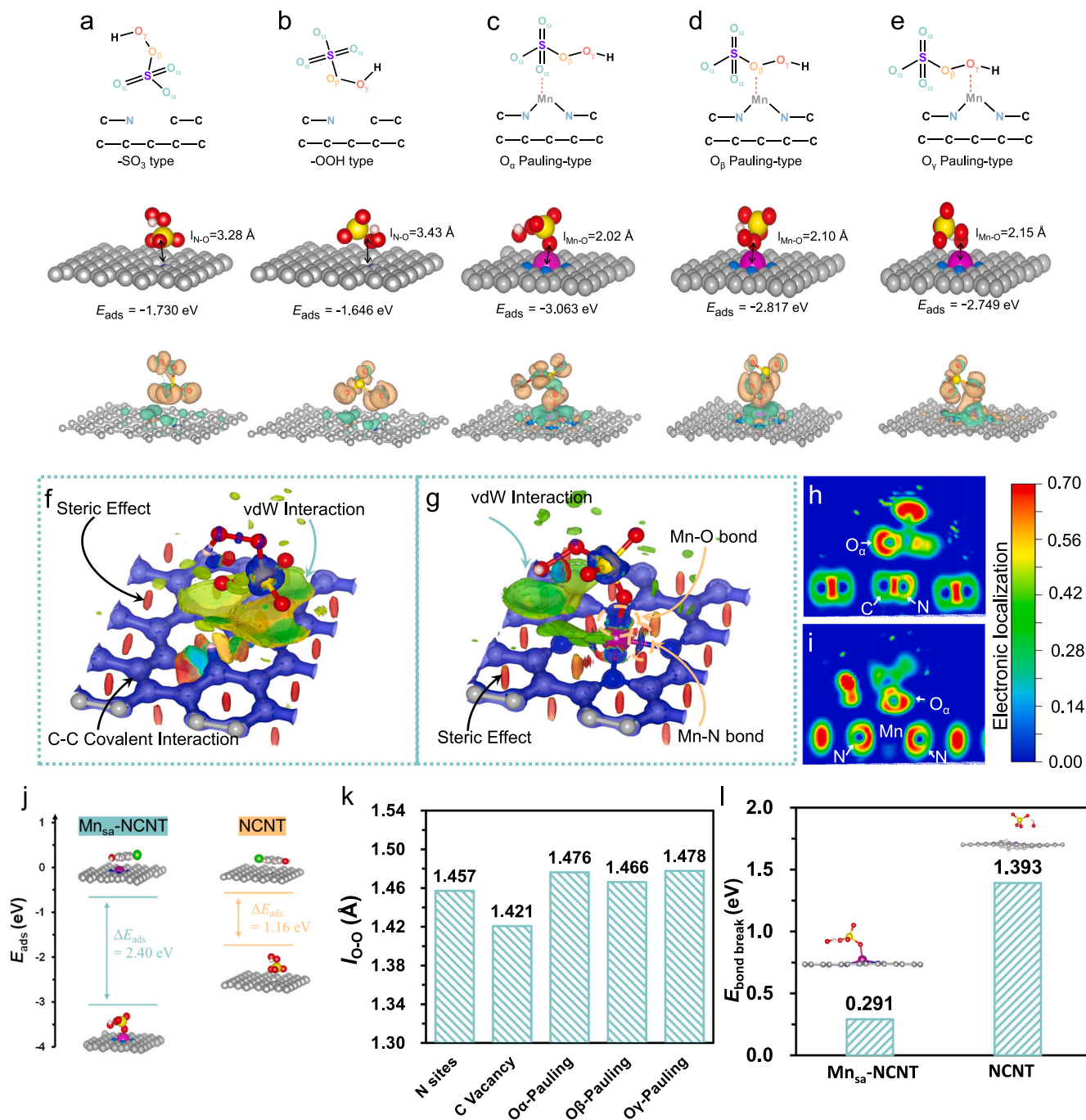
Fig. 6. Theoretical calculation of different interactions. Schematic diagram, optimized configurations and charge density difference with isosurface value of 0.002 e/Bohr^3 (cyan stands for electron depletion and yellow for electron accumulation) of different interaction configurations: (**a**) -SO$_3$ type; (**b**) -OOH type; (**c**) O$_\alpha$-Pauling type; (**d**) O$_\beta$-Pauling type; (**e**) O$_\gamma$-Pauling type. DORI surface colored by *sign(λ_2)ρ* of (**f**) -SO$_3$ type and (**g**) O$_\alpha$-Pauling type. ELF map on the plane of (**h**) -SO$_3$ type and (**i**) O$_\alpha$-Pauling type. (**j**) The difference between PMS and 4-CP adsorption on Mn-N$_4$ site and N site. (**k**) The lengths of O-O bond of PMS molecule after adsorption on the catalyst surface. (**l**) bond breakage energy of O-O bond after adsorption on Mn-N$_4$ site and N site.

After clarifying the nature of the different interactions at the interface, we further examined the effect of different interactions on PMS activation. The electron density difference illuminates the superiority of the inner-sphere interaction (Figs. 6a-6e and Fig. S44-48). In heterogeneous PMS catalysis, the PMS activation rate is determined by the electron transfer from the catalyst surface to the empty orbitals of PMS. After PMS adsorption, the electron transfer from Mn$_{sa}$-NCNT surface to PMS is more significant (O$_\alpha$-Pauling type, O$_\beta$-Pauling type and O$_\gamma$-Pauling type) as compared with that from NCNT to PMS (-SO$_3$ type and –OOH type). PMS adsorption via inner-sphere interaction lengthens the O-O bond lengths compared to the outer-sphere interaction (Fig. 6k), which promotes bond breakage and PMS activation. The bond breakage energies of the O-O bond following the adsorption of PMS on Mn$_{sa}$-NCNT and NCNT were calculated as 0.291 eV and 1.393 eV, respectively (Fig. 6l). This observation suggests that inner-sphere interactions play a beneficial role in facilitating PMS utilization. The above results demonstrate that the catalysis via inner-sphere interaction would result in more efficient PMS utilization and pollutant elimination, which is consistent with the results in Figs. 3c-3d. All the above results confirmed that inner-sphere interactions paly important role in not only reactant

adsorption but also reactant activation.

The applicability of the interfacial model to numerous single-atom catalysts was further verified using theoretical calculation tools. The metal centers chosen were Fe, Co and Cu, which are widely used in Fenton-like catalysis. As illustrated in Fig. S49-S55, Fe-N_4, Co-N_4 and Cu-N_4 moieties all exhibit strong adsorption of PMS with E_{ads} of -2.912, -2.683, -2.420 eV, respectively. The bond length of Fe-O, Co-O and Cu-O are 2.208, 2.016 and 2.208 Å, respectively. The DORI analysis similarly indicates chemical bonds are formed between the metal center and the O atom. The above results show that inner-sphere interactions are widespread in Fenton-like catalysis that based on single-atom catalysts and peroxymonosulfate. Meanwhile, the 4-CP adsorption on metal-N_4 sites is also investigated (Fig. S56-S62). The shortest distances between metal-N_4 sites and 4-CP molecules are all beyond the bonding distance and DORI analysis shows vdW interaction between 4-CP and metal-N_4 sites, demonstrating that outer-sphere interactions dominate 4-CP adsorption on single atom catalyst. Therefore, the proposed interaction model is suitable to illustrate the superiority of single-atom catalysts in Fenton-like catalysis and expected to help in understanding more of the interfacial behaviors in other heterogeneous Fenton-like catalysis.

4. Conclusion

In summary, we selected atomically-dispersed Mn on NCNT (Mn_{sa}-NCNT) and N-doped carbon nanotubes as research platforms to trace the difference of interaction behaviors at the solid/liquid interface in Fenton-like catalysis. The difference in electronic structure of Mn-N_4 moieties and the N-doped carbon sp^2 framework causes Mn_{sa}-NCNT to adsorb and utilize PMS more efficiently even in the presence of coexisting substances. Therefore, Mn_{sa}-NCNT exhibits higher PMS consumption in the presence of 4-CP than NCNT though NCNT could adsorb more PMS in the absence of 4-CP. The theoretical model specifies that atomically-dispersed Mn adsorbs PMS through inner-sphere interaction and NCNT adsorbs PMS through outer-sphere interaction. The new peak in the O 1 s XPS spectra of Mn_{sa}-NCNT/PMS and the results of EXAFS strongly support the formation of a Mn-O chemical bond. The nature of the inner-sphere interaction between Mn_{sa}-NCNT and PMS is ionic bonding and that of the outer-sphere interaction between NCNT and PMS is van del Waals interactions.

The proposed theoretical interface model advances our understanding of interfacial reactions in Fenton-like processes and should inspire subsequent research to explore the underlying mechanism of Fenton-like catalysis in depth from an interfacial perspective. The overlooked effect of interactions between the catalyst surface and reactants in solution should be reconsidered. In addition, these findings could inspire new designs for more efficient, economically affordable water treatment nanotechnologies. For instance, rather than simply increasing the adsorption capacity, robustness of oxidant adsorption should be improved. More active sites for oxidant adsorption via inner sphere interaction can be introduced into catalyst surface to enhance the utilization and activation of oxidants.

CRediT authorship contribution statement

Yue Qingyan: Funding acquisition, Supervision. **Gao Yue:** Formal analysis, Funding acquisition, Investigation, Visualization, Writing – review & editing. **Gao Baoyu:** Conceptualization, Funding acquisition, Resources, Supervision, Writing – review & editing. **Pijun Duan:** Conceptualization, Data curation, Formal analysis, Investigation, Methodology, Visualization, Writing – original draft. **Li Mingxue:** Investigation, Methodology, Visualization. **Xu Xing:** Methodology, Writing – review & editing.

Declaration of Competing Interest

The authors declare that they have no known competing financial interests or personal relationships that could have appeared to influence the work reported in this paper.

Data Availability

Data will be made available on request.

Appendix A. Supporting information

Supplementary data associated with this article can be found in the online version at doi:10.1016/j.apcatb.2023.123619.

References

[1] J. Xu, X. Zheng, Z. Feng, Z. Lu, Z. Zhang, W. Huang, Y. Li, D. Vuckovic, Y. Li, S. Dai, G. Chen, K. Wang, H. Wang, J.K. Chen, W. Mitch, Y. Cui, Organic wastewater treatment by a single-atom catalyst and electrolytically produced H2O2, Nat. Sustain. 4 (2020) 233–241.

[2] L. Wu, X.-W. Qiu, T. Wang, K. Tao, L.-J. Bao, E.Y. Zeng, Water quality and organic pollution with health risk assessment in china: a short review, ACS EST Water 2 (2022) 1279–1288.

[3] Y. Chen, L. Zang, G. Shen, M. Liu, W. Du, J. Fei, L. Yang, L. Chen, X. Wang, W. Liu, M. Zhao, Resolution of the ongoing challenge of estimating nonpoint source neonicotinoid pollution in the yangtze river basin using a modified mass balance approach, Environ. Sci. Technol. 53 (2019) 2539–2548.

[4] B.C. Hodges, E.L. Cates, J.H. Kim, Challenges and prospects of advanced oxidation water treatment processes using catalytic nanomaterials, Nat. Nanotechnol. 13 (2018) 642–650.

[5] L.M. Gilbertson, J.B. Zimmerman, D.L. Plata, J.E. Hutchison, P.T. Anastas, Designing nanomaterials to maximize performance and minimize undesirable implications guided by the Principles of Green Chemistry, Chem. Soc. Rev. 44 (2015) 5758–5777.

[6] K. Yin, Y. Shang, D. Chen, B. Gao, Q. Yue, X. Xu, Redox potentials of pollutants determining the dominate oxidation pathways in manganese single-atom catalyst (Mn-SAC)/peroxymonosulfate system: Selective catalytic mechanisms for versatile pollutants, Appl. Catal. B: Environ. 338 (2023), 123029.

[7] K. Yin, R. Wu, Y. Shang, D. Chen, Z. Wu, X. Wang, B. Gao, X. Xu, Microenvironment modulation of cobalt single-atom catalysts for boosting both radical oxidation and electron-transfer process in Fenton-like system, Appl. Catal. B: Environ. 329 (2023), 122558.

[8] M. Ma, F. Xu, J. Liu, B. Li, Z. Liu, B. Gao, Q. Li, Insights into S-doped iron-based carbonaceous nanocomposites with enhanced activation of persulfate for rapid degradation of organic pollutant, Chemosphere 335 (2023), 139006.

[9] Z. Liu, S. Pan, F. Xu, Z. Wang, C. Zhao, X. Xu, B. Gao, Q. Li, Revealing the fundamental role of MoO2 in promoting efficient and stable activation of persulfate by iron carbon based catalysts: efficient Fe2+/Fe3+ cycling to generate reactive species, Water Res 225 (2022), 119142.

[10] S. Enami, Y. Sakamoto, A.J. Colussi, Fenton chemistry at aqueous interfaces, Proc. Natl. Acad. Sci. USA 111 (2014) 623–628.

[11] Y.J. Zhang, J.J. Chen, G.X. Huang, W.W. Li, H.Q. Yu, M. Elimelech, Distinguishing homogeneous advanced oxidation processes in bulk water from heterogeneous surface reactions in organic oxidation, Proc. Natl. Acad. Sci. USA 120 (2023), e2302407120.

[12] J. Song, N. Hou, X. Liu, M. Antonietti, P. Zhang, R. Ding, L. Song, Y. Wang, Y. Mu, Asymmetrically coordinated CoB(1) N(3) moieties for selective generation of high-valence Co-oxo species via coupled electron-proton transfer in fenton-like reactions, Adv. Mater. (2023), e2209552.

[13] Z. Wang, W. Qiu, S.Y. Pang, Q. Guo, C. Guan, J. Jiang, Aqueous iron(IV)-oxo complex: an emerging powerful reactive oxidant formed by iron(ii)-based advanced oxidation processes for oxidative water treatment, Environ. Sci. Technol. (2022).

[14] W. Ren, C. Cheng, P. Shao, X. Luo, H. Zhang, S. Wang, X. Duan, Origins of electron-transfer regime in persulfate-based nonradical oxidation processes, Environ. Sci. Technol. (2021).

[15] X. Mi, P. Wang, S. Xu, L. Su, H. Zhong, H. Wang, Y. Li, S. Zhan, Almost 100% peroxymonosulfate conversion to singlet oxygen on single-atom CoN2+2 sites, Angew. Chem. Int Ed. Engl. 60 (2021) 4588–4593.

[16] R. Su, N. Li, Z. Liu, X. Song, W. Liu, B. Gao, W. Zhou, Q. Yue, Q. Li, Revealing the generation of high-valent cobalt species and chlorine dioxide in the Co3O4-activated chlorite process: insight into the proton enhancement effect, Environ. Sci. Technol. 57 (2023) 1882–1893.

[17] J. Carrasco, A. Hodgson, A. Michaelides, A molecular perspective of water at metal interfaces, Nat. Mater. 11 (2012) 667–674.

[18] O.M. Magnussen, A. Gross, Toward an atomic-scale understanding of electrochemical interface structure and dynamics, J. Am. Chem. Soc. 141 (2019) 4777–4790.

[19] G. Gonella, E.H.G. Backus, Y. Nagata, D.J. Bonthuis, P. Loche, A. Schlaich, R. R. Netz, A. Kuhnle, I.T. McCrum, M.T.M. Koper, M. Wolf, B. Winter, G. Meijer, R. K. Campen, M. Bonn, Water at charged interfaces, Nat. Rev. Chem. 5 (2021) 466–485.

[20] E. Barry, R. Burns, W. Chen, G.X. De Hoe, J.M.M. De Oca, J.J. de Pablo, J. Dombrowski, J.W. Elam, A.M. Felts, G. Galli, J. Hack, Q. He, X. He, E. Hoenig, A. Iscen, B. Kash, H.H. Kung, N.H.C. Lewis, C. Liu, X. Ma, A. Mane, A.B. F. Martinson, K.L. Mulfort, J. Murphy, K. Molhave, P. Nealey, Y. Qiao, V. Rozyyev, G.C. Schatz, S.J. Sibener, D. Talapin, D.M. Tiede, M.V. Tirrell, A. Tokmakoff, G. A. Voth, Z. Wang, Z. Ye, M. Yesibolati, N.J. Zaluzec, S.B. Darling, Advanced materials for energy-water systems: the central role of water/solid interfaces in adsorption, reactivity, and transport, Chem. Rev. 121 (2021) 9450–9501.

[21] C. Xie, Z. Niu, D. Kim, M. Li, P. Yang, Surface and interface control in nanoparticle catalysis, Chem. Rev. 120 (2020) 1184–1249.

[22] R. Kusaka, S. Nihonyanagi, T. Tahara, The photochemical reaction of phenol becomes ultrafast at the air-water interface, Nat. Chem. 13 (2021) 306–311.

[23] Y. Shang, X. Xu, B. Gao, S. Wang, X. Duan, Single-atom catalysis in advanced oxidation processes for environmental remediation, Chem. Soc. Rev. 50 (2021) 5281–5322.

[24] X. Li, X. Huang, S. Xi, S. Miao, J. Ding, W. Cai, S. Liu, X. Yang, H. Yang, J. Gao, J. Wang, Y. Huang, T. Zhang, B. Liu, Single cobalt atoms anchored on porous N-doped graphene with dual reaction sites for efficient fenton-like catalysis, J. Am. Chem. Soc. 140 (2018) 12469–12475.

[25] S. Weon, D. Huang, K. Rigby, C. Chu, X. Wu, J.-H. Kim, Environmental materials beyond and below the nanoscale: single-atom catalysts, ACS EST Eng. (2020).

[26] Y. Gao, T. Wu, C. Yang, C. Ma, Z. Zhao, Z. Wu, S. Cao, W. Geng, Y. Wang, Y. Yao, Y. Zhang, C. Cheng, Activity trends and mechanisms in peroxymonosulfate-assisted catalytic production of singlet oxygen over atomic metal-N-C catalysts, Angew. Chem. Int Ed. Engl. 60 (2021) 22513–22521.

[27] B. Wang, C. Cheng, M. Jin, J. He, H. Zhang, W. Ren, J. Li, D. Wang, Y. Li, A site distance effect induced by reactant molecule matchup in single-atom catalysts for fenton-like reactions, Angew. Chem. Int Ed. Engl. 61 (2022), e202207268.

[28] Z. Wang, E. Almatrafi, H. Wang, H. Qin, W. Wang, L. Du, S. Chen, G. Zeng, P. Xu, Cobalt single atoms anchored on oxygen-doped tubular carbon nitride for efficient peroxymonosulfate activation: simultaneous coordination structure and morphology modulation, Angew. Chem. Int Ed. Engl. (2022), e202202338.

[29] Q. Fu, X. Bao, Surface chemistry and catalysis confined under two-dimensional materials, Chem. Soc. Rev. 46 (2017) 1842–1874.

[30] D. Zhao, Z. Zhuang, X. Cao, C. Zhang, Q. Peng, C. Chen, Y. Li, Atomic site electrocatalysts for water splitting, oxygen reduction and selective oxidation, Chem. Soc. Rev. 49 (2020) 2215–2264.

[31] Z. Li, S. Ji, Y. Liu, X. Cao, S. Tian, Y. Chen, Z. Niu, Y. Li, Well-defined materials for heterogeneous catalysis: from nanoparticles to isolated single-atom sites, Chem. Rev. 120 (2020) 623–682.

[32] X. Chen, X. Duan, W.-D. Oh, P.-H. Zhang, C.-T. Guan, Y.-A. Zhu, T.-T. Lim, Insights into nitrogen and boron-co-doped graphene toward high-performance peroxymonosulfate activation: maneuverable N-B bonding configurations and oxidation pathways, Appl. Catal. B: Environ. 253 (2019) 419–432.

[33] Y. Zhao, L. Yu, C. Song, Z. Chen, F. Meng, M. Song, Selective degradation of electron-rich organic pollutants induced by CuO@Biochar: the key role of outer-sphere interaction and singlet oxygen, Environ. Sci. Technol. (2022).

[34] Y. Min, X. Zhou, J.J. Chen, W. Chen, F. Zhou, Z. Wang, J. Yang, C. Xiong, Y. Wang, F. Li, H.Q. Yu, Y. Wu, Integrating single-cobalt-site and electric field of boron nitride in dechlorination electrocatalysts by bioinspired design, Nat. Commun. 12 (2021) 303.

[35] X. Wu, J.-H. Kim, Outlook on single atom catalysts for persulfate-based advanced oxidation, ACS EST Eng. (2022).

[36] G. Kresse, J. Furthmuller, Efficiency of ab-initio total energy calculations for metals and semiconductors using a plane-wave basis set, Comput. Mater. Sci. 6 (1996) 15–50.

[37] G. Kresse, J. Furthmuller, Efficient iterative schemes for ab initio total-energy calculations using a plane-wave basis set, Phys. Rev. B 54 (1996) 11169–11186.

[38] J.P. Perdew, K. Burke, M. Ernzerhof, Generalized gradient approximation made simple, Phys. Rev. Lett. 78 (1997), 1396-1396.

[39] G. Kresse, D. Joubert, From ultrasoft pseudopotentials to the projector augmented-wave method, Phys. Rev. B 59 (1999) 1758–1775.

[40] S. Grimme, J. Antony, S. Ehrlich, H. Krieg, A consistent and accurate ab initio parametrization of density functional dispersion correction (DFT-D) for the 94 elements H-Pu, J. Chem. Phys. 132 (2010), 154104.

[41] P. de Silva, C. Corminboeuf, Simultaneous visualization of covalent and noncovalent interactions using regions of density overlap, J. Chem. Theory Comput. 10 (2014) 3745–3756.

[42] F. Chen, L.L. Liu, J.H. Wu, X.H. Rui, J.J. Chen, Y. Yu, Single-atom iron anchored tubular g-C3 N4 catalysts for ultrafast fenton-like reaction: roles of high-valency iron-oxo species and organic radicals, Adv. Mater. 34 (2022), e2202891.

[43] E. Zhang, L. Tao, J. An, J. Zhang, L. Meng, X. Zheng, Y. Wang, N. Li, S. Du, J. Zhang, D. Wang, Y. Li, Engineering the local atomic environments of indium single-atom catalysts for efficient electrochemical production of hydrogen peroxide, Angew. Chem. Int Ed. Engl. 61 (2022), e202117347.

[44] K. Qian, H. Chen, W. Li, Z. Ao, Y.N. Wu, X. Guan, Single-atom Fe catalyst outperforms its homogeneous counterpart for activating peroxymonosulfate to achieve effective degradation of organic contaminants, Environ. Sci. Technol. (2021).

[45] J. Zhang, Y. Sun, J. Zhu, Z. Kou, P. Hu, L. Liu, S. Li, S. Mu, Y. Huang, Defect and pyridinic nitrogen engineering of carbon-based metal-free nanomaterial toward oxygen reduction, Nano Energy 52 (2018) 307–314.

[46] X. Duan, W. Tian, H. Zhang, H. Sun, Z. Ao, Z. Shao, S. Wang, sp2/sp3 framework from diamond nanocrystals: a key bridge of carbonaceous structure to carbocatalysis, ACS Catal. 9 (2019) 7494–7519.

[47] P. Duan, J. Pan, W. Du, Q. Yue, B. Gao, X. Xu, Activation of peroxymonosulfate via mediated electron transfer mechanism on single-atom Fe catalyst for effective organic pollutants removal, Appl. Catal. B: Environ. 299 (2021).

[48] W. Ren, L. Xiong, X. Yuan, Z. Yu, H. Zhang, X. Duan, S. Wang, Activation of peroxydisulfate on carbon nanotubes: electron-transfer mechanism, Environ. Sci. Technol. 53 (2019) 14595–14603.

[49] G. Nardi, I. Manet, S. Monti, M.A. Miranda, V. Lhiaubet-Vallet, Scope and limitations of the TEMPO/EPR method for singlet oxygen detection: the misleading role of electron transfer, Free Radic. Biol. Med 77 (2014) 64–70.

[50] W. Ren, G. Nie, P. Zhou, H. Zhang, X. Duan, S. Wang, The intrinsic nature of persulfate activation and N-doping in carbocatalysis, Environ. Sci. Technol. 54 (2020) 6438–6447.

[51] W. Ren, L. Xiong, G. Nie, H. Zhang, X. Duan, S. Wang, Insights into the electron-transfer regime of peroxydisulfate activation on carbon nanotubes: the role of oxygen functional groups, Environ. Sci. Technol. 54 (2020) 1267–1275.

[52] M. Yang, Z. Hou, X. Zhang, B. Gao, Y. Li, Y. Shang, Q. Yue, X. Duan, X. Xu, Unveiling the origins of selective oxidation in single-atom catalysis via Co-N4-C intensified radical and nonradical pathways, Environ. Sci. Technol. 56 (2022) 11635–11645.

[53] T.E. Payne, V. Brendler, M. Ochs, B. Baeyens, P.L. Brown, J.A. Davis, C. Ekberg, D. A. Kulik, J. Lutzenkirchen, T. Missana, Y. Tachi, L.R. Van Loon, S. Altmann, Guidelines for thermodynamic sorption modelling in the context of radioactive waste disposal, Environ. Model. Softw. 42 (2013) 143–156.

[54] S.M. Abozeid, E.M. Snyder, T.Y. Tittiris, C.M. Steuerwald, A.Y. Nazarenko, J. R. Morrow, Inner-sphere and outer-sphere water interactions in Co(II) paraCEST agents, Inorg. Chem. 57 (2018) 2085–2095.

[55] J.A. Keith, D.C. Behenna, N. Sherden, J.T. Mohr, S. Ma, S.C. Marinescu, R. J. Nielsen, J. Oxgaard, B.M. Stoltz, W.A. Goddard 3rd, The reaction mechanism of the enantioselective Tsuji allylation: inner-sphere and outer-sphere pathways, internal rearrangements, and asymmetric C-C bond formation, J. Am. Chem. Soc. 134 (2012) 19050–19060.

[56] X. Qin, T. Vegge, H.A. Hansen, Cation-coordinated inner-sphere CO(2) electroreduction at Au-water interfaces, J. Am. Chem. Soc. 145 (2023) 1897–1905.

[57] J. Lee, U. von Gunten, J.H. Kim, Persulfate-based advanced oxidation: critical assessment of opportunities and roadblocks, Environ. Sci. Technol. 54 (2020) 3064–3081.

[58] J. Lu, N.S. Khetrapal, J.A. Johnson, X.C. Zeng, J. Zhang, "pi-Hole-pi" interaction promoted photocatalytic hydrodefluorination via inner-sphere electron transfer, J. Am. Chem. Soc. 138 (2016) 15805–15808.

[59] P.S. Bagus, E. Ilton, C.J. Nelin, Extracting chemical information from XPS spectra: a perspective, Catal. Lett. 148 (2018) 1785–1802.